ACS Catalysis

pubs.acs.org/acscatalysis

Research Article

Surface Decoration of Platinum Catalysts by ZrO_{2-x} Nanoclusters for Durable Fuel Cell Applications

Nagappan Ramaswamy,* Zixiao Shi, Barr Zulevi, Geoff McCool, Nathan P. Mellott, Anusorn Kongkanand, Swami Kumaraguru, Michele L. Ostraat, David A. Muller, Nancy N. Kariuki, Deborah J. Myers, and A. Jeremy Kropf

Cite This: *ACS Catal.* 2024, 14, 4441−4452

Read Online

ACCESS | Metrics & More | Article Recommendations | Supporting Information

ABSTRACT: Improving the activity and durability of carbon-supported platinum catalysts for the oxygen-reduction reaction (ORR) in acidic electrolytes is crucial to reducing the high overpotentials and power loss over time in proton-exchange membrane fuel cells (PEMFCs). We found that platinum nanoparticle catalyst deposited on an engineered carbon support in the presence of zirconium enabled higher ORR activity and 25% better retention in electrochemically active surface area (ECSA), thereby improving durability. The use of zirconium precursor in the carbon synthesis process led to the formation of atomically dispersed Zr and ZrO_2 nanoparticles on the support. Upon Pt deposition and subsequent heat treatment, the ZrO_2 particles preferentially rearranged on and around the platinum nanoparticles in a chemically reduced form as zirconium suboxide (ZrO_{2-x}) surface-decorated nanoclusters, which mitigated Pt nanoparticle coarsening. Analysis of the here-to-fore unknown catalyst structure as well as its performance and durability in a PEM fuel cell membrane electrode assembly (MEA) is discussed.

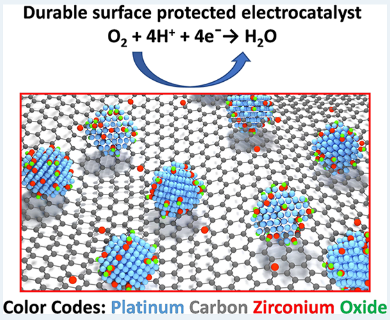

KEYWORDS: *oxygen-reduction reaction, proton-exchange membrane fuel cells, platinum nanoparticle, electrochemically active surface area, membrane electrode assembly*

Electrocatalysis of the oxygen-reduction reaction (ORR) on carbon-supported platinum (Pt/C) catalysts is crucial to the operation of PEMFCs as it is a determining factor in the performance, efficiency, durability, and cost of the electrochemical energy conversion system.[1−3] Despite tremendous work in precious group metal (PGM) free catalysts,[4] Pt-based catalysts remain the most active and industrially relevant materials as they enable the high-power density of ≥4 kW_{rated}/g_{PGM} at beginning of life (BOL) required for light-duty automotive applications.[1,5] The shift to a heavy-duty vehicle (HDV) applications demands a higher durability of 25,000 h of fuel cell operation, ≥68% efficiency at a PGM loading of ≤0.30 mg/cm^2 so as to decrease the total cost of ownership.[6] The United States Department of Energy (DOE) has established a 2025 HDV-combined end-of-life (EOL) PGM-specific power density target of 2.5 kW/g_{PGM} at 0.7 V_{rated},[7,8] while the Japanese New Energy & Industrial Development Organization (NEDO) has set a more aggressive 2030 target of 5.3 kW/g_{PGM}. These targets require a greater focus on improving the durability of Pt/C catalysts.

Fuel cell performance decreases over time primarily due to loss in Pt surface area and mass activity in the corrosive cathode environment.[9,10] Pt nanoparticles are thermodynamically prone to coarsening largely driven by the need to reduce surface energy.[11,12] Pt dissolution followed by either redeposition in the membrane[13] or in the cathode on larger Pt nanoparticles (electrochemical Ostwald ripening)[13−17] appears to be the dominant coarsening mechanism on porous carbon supports. On graphitized carbon supports with relatively ordered lattice planes, Pt adatom/particle migration followed by coalescence to form larger Pt nanoparticles coexists due to weaker Pt-carbon interactions as evidenced by the formation of elongated particles on degraded catalyst samples.[18−21] Loosely coordinated Pt edge atoms become mobile and undergo diffusion on the nanoparticle surface, thereby shifting the center of gravity of the particle leading to a collective result over time of particle diffusion of a few nanometers on the support.[22]

One approach to prevent Pt surface area loss is to anchor Pt on the support via stronger interactions to inhibit particle movement via steric stabilization.[23−26] In the field of heterogeneous catalysis, remarkable improvements in the prevention of catalyst sintering were demonstrated on supported precious metal nanoparticle catalysts using highly

Received: November 3, 2023
Revised: January 23, 2024
Accepted: February 28, 2024

ACS Publications

https://doi.org/10.1021/acscatal.3c05297

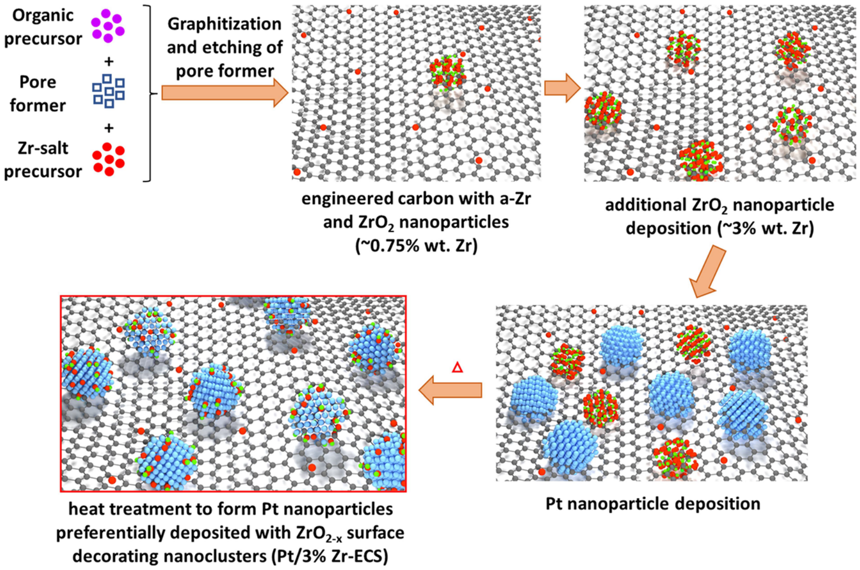

Figure 1. (a) General scheme for the synthesis of engineered carbon supported Pt nanoparticles preferentially deposited with surface decorating ZrO_{2-x} nanoclusters (color codes: gray—carbon, red – Zr, green—oxygen, blue – Pt).

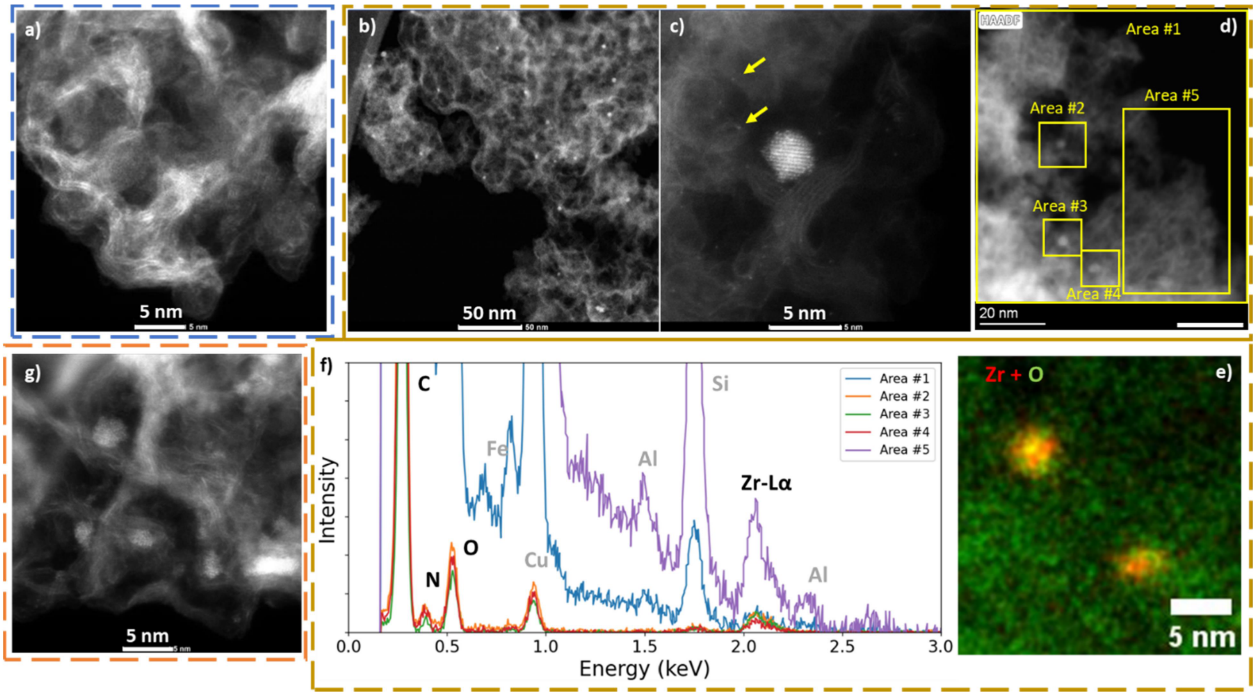

Figure 2. STEM images of (a) bare ECS carbon support, (b–f) 0.75% Zr-ECS support along with EDS maps, and (g) 3% Zr-ECS support. Arrows in (c) point to the presence of atomically dispersed Zr moieties on 0.75% Zr-ECS. (Si and Al signals are from the STEM-chamber that widely exists as dust, and Fe is a possible contaminant in ppm quantities in the carbon).

conformal, porous multilayer coatings of metal oxides, which feature a stronger degree of interaction.[22,27] Following similar approaches, improved retention of Pt surface area in dilute aqueous electrolytes was demonstrated with intentionally deposited protective silica overlayers,[28] atomic layer deposited zirconia nanolayers,[29] or selenium anchors.[23] In a realistic fuel cell MEA though, the overlayers are likely to decrease the Pt accessibility and hinder reactant (H^+/O_2) transport to the active site.[30,31] More careful anchoring approaches are required to demonstrate the viability in a PEMFC MEA.

In a recent article, we disseminated the results of a new class of carbon supports developed by Pajarito Powder with improved Pt dispersion characteristics and lower O_2 transport resistances. These carbon supports featured higher mesopore fraction in an open, accessible fashion for the dispersion of higher weight percent loading of Pt nanoparticles (up to 50% Pt) that enabled thinner catalyst layers at higher geometric Pt loadings (~0.2 to 0.3 mg_{Pt}/cm^2) and led to improved performance and durability characteristics across the entire polarization curve region.[32]

In this article, we expand on this new class of carbon supports and discuss a synthetic strategy that serendipitously deposited surface decorating ZrO_{2-x} nanoclusters on and around Pt nanoparticles, which mitigated nanoparticle

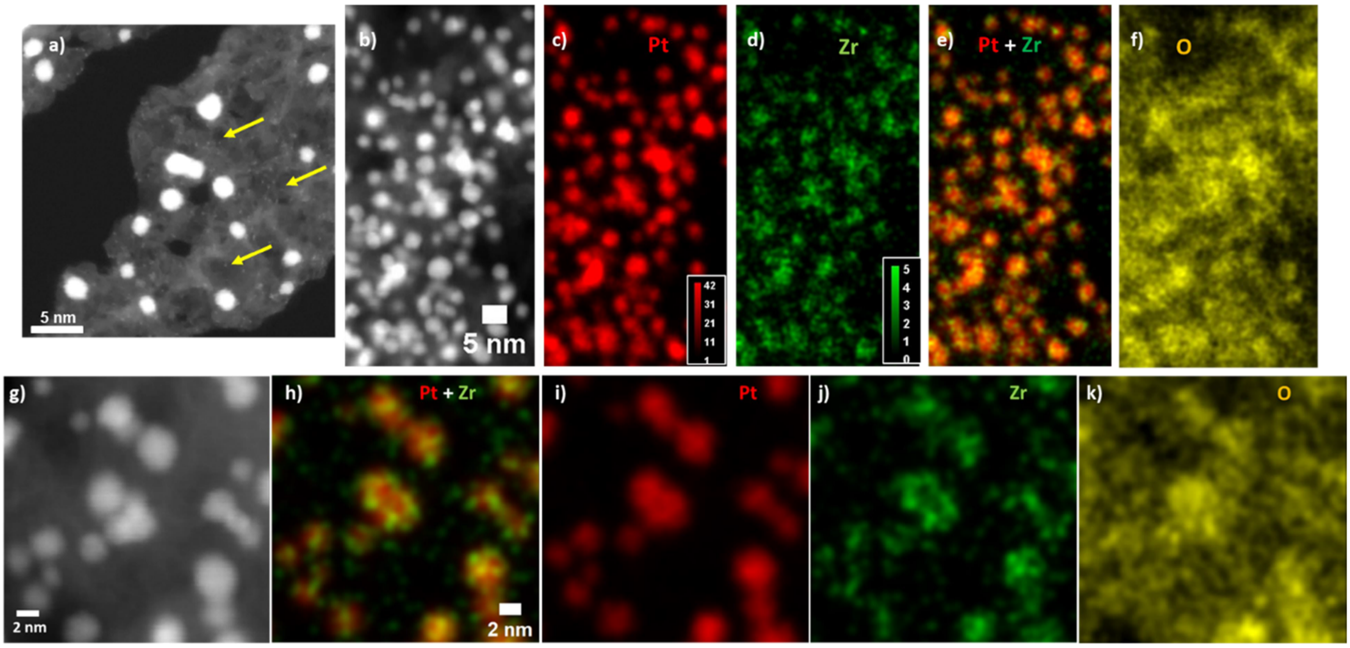

Figure 3. (a, b, g) HAADF STEM images and (c−f, h−k) EDS maps of the elements in Pt/3% Zr-ECS (predoped) catalyst heat treated to 800 °C temperature. Yellow arrows in (a) point to atomically dispersed Zr on carbon.

coarsening, thereby enabling higher surface area retention in a PEMFC MEA. ZrO_{2-x} nanoclusters were observed to be in a stable chemical form with submonolayer coverages on the Pt surface, thereby providing unhindered access to the reactants. Improved mass activity and ECSA retention of the Zr-modified catalyst enabled improved retention of cell voltage over 90,000 cycles of a catalyst-specific accelerated stress test (AST) in a PEMFC MEA. The novel nanostructure catalyst design presents new opportunities for durable fuel cell ORR electrocatalysts in HDV truck applications.

STRUCTURE OF PT CATALYST WITH ZRO$_{2-x}$ SURFACE DECORATING NANOCLUSTERS

The general scheme of synthesizing a Pt catalyst on an Engineered Catalyst Support (ECS) doped with Zr/ZrO_2 is shown in Figure 1. A mixture of a nitrogen-rich organic precursor such as melamine for the carbon along with fumed silica as the pore-forming agent and zirconium nitrate as Zr precursor required for 0.75% Zr by weight on carbon, was subjected to pyrolysis at high temperature to synthesize the carbon support.[33−35] The silica template was then removed via hydrofluoric acid etching, which resulted in a porous, ECS featuring doped Zr in two different chemical forms: (i) atomically dispersed Zr (a-Zr) in the graphitic lattice and (ii) ZrO_2 nanoparticles. This Zr-predoped carbon support is labeled as 0.75% Zr-ECS. An additional 2.25% Zr by weight was deposited using $Zr(NO_3)_4$ precipitation and reduction on 0.75% Zr-ECS leading to a total Zr content of ∼3% by weight on carbon.[33,34] Pt nanoparticles were then deposited subsequently at a weight loading of either 30 or 50% on carbon via a wet chemical route, leading to the coexistence of Pt, a-Zr, and ZrO_2 nanoparticles on the support. Details of the general synthesis route and the precursors used are provided in the patent literature.[33,34] The catalyst was then subjected to heat treatment (HT) at 800 °C in a nitrogen gas atmosphere, wherein the ZrO_2 nanoparticles on the support were found to disintegrate and preferentially redeposit on and around the Pt nanoparticles as surface decorating nanoclusters in a reduced chemical form as zirconium suboxides (ZrO_{2-x}). This Zr-predoped carbon support and the catalyst are labeled as nominal 3% Zr-ECS and 30% Pt/3% Zr-ECS, respectively. The physicochemical properties, microscopic structure, and electrochemical diagnostics of this catalyst in a PEMFC MEA were studied using multiple characterization techniques and are discussed in this manuscript in comparison to Pt on a nondoped ECS catalyst (Pt/ECS) and a KetjenBlack-EC300J high surface area carbon (HSC) catalyst referred throughout as Pt/HSC.

The evolution of the structure of ECS material predoped with $a\text{-}Zr/ZrO_2$ at various stages of the synthesis was studied, as shown in Figure 2 (and Supporting Information Figure S1), using scanning-transmission electron microscopy (STEM) coupled with electron energy loss spectroscopy (EELS) or energy dispersive spectra (EDS). The nondoped ECS material shows an ordered graphitic surface but with short-range order in surface carbon lattice planes (∼3 to 8 layers of graphene) around the mesopore regions (Figure 2a). Figure 2b−f shows the high-angle annular dark field (HAADF) STEM-EDS of 0.75% Zr-ECS predoped material at various magnifications. The carbon support features Zr in two different chemical forms, as identified by EDS/EELS spectroscopy. EDS spectra confirmed that the ∼2−3 nm particles as ZrO_2 crystalline nanoparticles dispersed on the carbon support (Figure 2d,e). Further, local-EDS spectra with an electron probe positioned in *Area #5* of the image in Figure 2d where there are no apparent ZrO_2 nanoparticles suggested the distinctly bright spots (pointed by yellow arrows in Figure 2c) to be atomically dispersed Zr species on the graphitic lattice. EDS map indicates the presence of nitrogen, which we believe to be doped in the carbon support and not associated with Zr, as evidenced by the X-ray photoelectron spectroscopy (XPS) discussed later. The 3% Zr-ECS sample showed the formation of additional ZrO_2 nanoparticles on the support as observed in

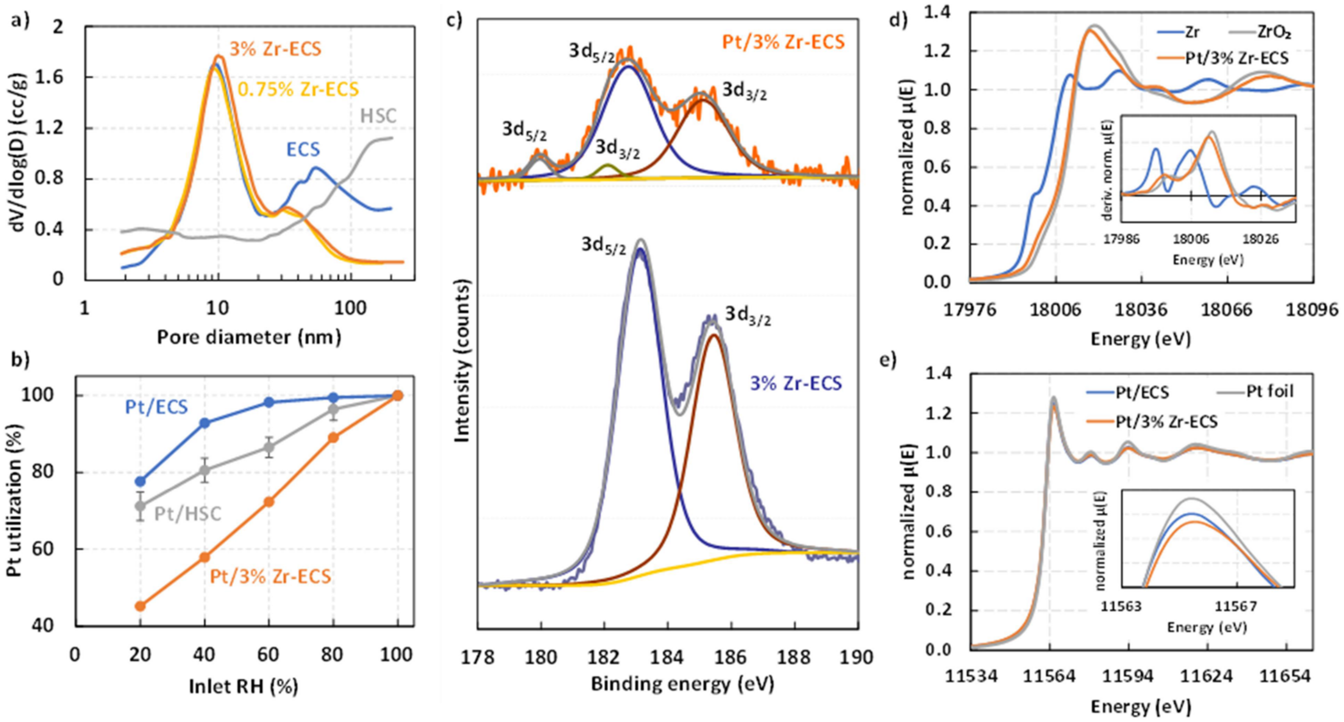

Figure 4. (a) N_2 adsorption pore size distribution, (b) Pt utilization measured from CO_{ad} stripping as a function of inlet RH of 50% Pt catalysts, (c) Zr 3d XPS profiles and the corresponding fits, (d) Zr K-edge XANES profiles showing Zr and m-ZrO_2 standard reference compounds along with in situ Pt/3% Zr-ECS catalyst (data averaged from 0.1 to 0.9 V vs RHE in argon-purged 0.1 M $HClO_4$); inset shows the derivative of normalized absorption in the edge region and (e) in situ Pt L_3-edge XANES profiles of Pt/ECS and Pt/3% Zr-ECS catalysts at 0.5 V vs RHE in argon-purged 0.1 M $HClO_4$ along with the Pt foil standard; inset shows magnified image of the white line region.

the HAADF-STEM images shown in Figure 2g and EELS mapping shown in Figure S1.

The Pt catalyst deposited on nondoped ECS support shows a uniform dispersion of spherical Pt nanoparticles (Figure S2). STEM-EDS images collected immediately after Pt deposition on the 3% Zr-ECS carbon support *(prior to any heat treatment)* show the juxtaposition of Pt nanoparticles with a-Zr and intact ZrO_2 nanoparticles (Figure S3). Figure 3 shows the HAADF-STEM-EDS images of the 30% Pt/3% Zr-ECS catalyst *subjected to heat treatment.* First, the Pt nanoparticles that are ∼3 nm in size are evenly distributed on the carbon support against the backdrop of atomically dispersed Zr moieties (marked by yellow arrows in Figure 3). Interestingly, after heat treatment to 800 °C, while the total Zr content was unchanged, the larger ZrO_2 nanoparticles that were intact before heat treatment were no longer visible in the catalyst. The ZrO_2 nanoparticles had disintegrated and were found to be preferentially deposited on and around Pt nanoparticles as shells as seen by the Pt, Zr, and O EDS maps (see zoomed-in regions shown in Figure 3g−k). Zr and O EDS signals were observed to be associated with Pt nanoparticles mostly present on and around the Pt as surface decorating nanoclusters. Pt/Zr atomic ratio was found to be 7.7 ± 1.0 from STEM-EDS and ICP-MS measurements of the catalyst (Table S1).

■ ENGINEERED CARBON SUPPORT STRUCTURE

Figure 4a shows the N_2 adsorption pore size profiles of the engineered carbon support prior to Pt deposition (see Figure S4 for N_2 adsorption−desorption isotherms, micropore analysis profile, X-ray diffraction profiles, and Table S2 for the surface areas). HSC support has higher differential adsorption in the micropore area with an almost unchanging value up to 20 nm pores and then a slow rise to 200 nm pores with a total surface area of 837 m^2/g. ECS support with and without Zr doping shows a bimodal distribution in pore size with a dominant peak in adsorption at 9−10 nm pores, indicating their mesoporous character and a macropore peak at ∼30−80 nm. The macropore peak is quite subdued for the Zr-predoped ECS samples. 0.75% Zr-ECS has a ∼19% higher total surface area (953 m^2/g) than nondoped ECS (804 m^2/g), mostly attributable to an increase in the micropores (≲2 nm) and smaller mesopores (2 to 5 nm) created due to the presence of Zr during the graphitization process of the carbon support. The addition of excess 2.25% ZrO_2 nanoparticles on the 0.75% Zr-ECS carbon decreases the surface area by ∼5% to 903 m^2/g. Further, the N_2 adsorption profiles (Figure S4) of the ECS materials indicate a Type IV isotherm with an ordered mesopore character as observed from an increase in uptake at $0.6 < p/p^0 < 0.9$.[36,37] The level of disorder of the carbon was investigated using Raman spectroscopy (Figure S4, Table S1) via the intensity ratio (I_D/I_G) of disorder (D-band, 1300 cm^{-1}) and graphitic peaks (G-band, 1550 cm^{-1}). ECS support with and without Zr predoping shows a lower disordered carbon content with relatively well-ordered graphitic planes with an I_D/I_G peak ratio of ∼1.05 compared to 1.19 for HSC support in good agreement with the STEM images.[36] Water uptake on the carbon supports suggests that ECS materials with and without Zr dopants have an earlier onset in water partial pressure ($p/p^0 = 0.2$) and a higher water uptake compared to the HSC support ($p/p^0 = 0.6$), indicating that ECS is likely more hydrophilic in nature (Figure S5).

Figure 4b shows the electrochemical oxidative stripping of adsorbed CO (CO_{ad}) on Pt at BOL as a function of relative humidity (RH) to determine the location distribution of Pt

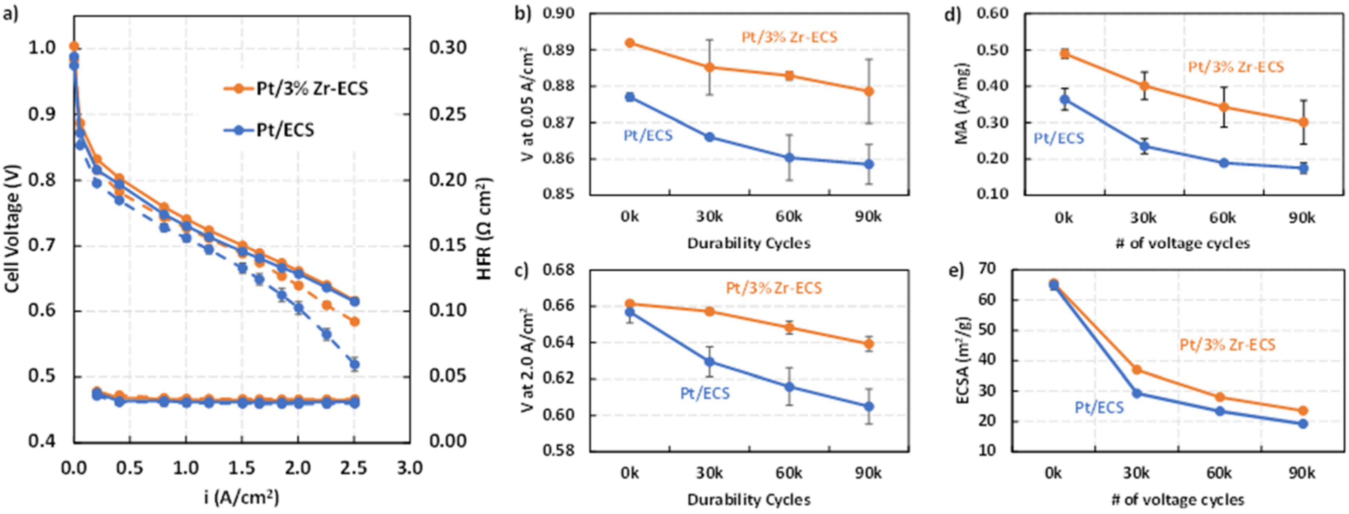

Figure 5. Plots showing the impact of Zr-dopant on 30% Pt catalyst from fuel cell MEA measurements: (a) H_2/air polarization curves measured at BOL (solid lines) and at EOT after 90,000 catalyst AST cycles (dashed lines). Cell voltages at (b) 0.05 A/cm^2 and (c) 2.0 A/cm^2, (d) mass activity, and (e) cathode ECSA all as a function of the number of AST cycles. Polarization curves were measured at 94 °C, 100% RH, and 250 kPa back pressure in a 5 cm^2 differential cell at 0.2 mg$_{Pt}$/cm^2 cathode loading.

nanoparticles with respect to the carbon pore structure.[38,39] All catalysts show an increase in Pt utilization with increasing RH, as expected, due to the condensation of water on the catalyst/ionomer surface, thereby connecting ionomer regions and creating proton transport pathways.[40,41] At a low RH of 20%, Pt/ECS and Pt/HSC catalysts show a relatively higher Pt accessibility of 71 to 77%, indicating the presence of a significant number of Pt nanoparticles on the external surface in contact with a continuous ionomer film. The Pt/3% Zr-ECS sample shows a significant drop in Pt accessibility (~34% at 20% RH) due to the use of Zr in the carbon synthesis process that leads to the formation of micro- and mesopores in good agreement with the N_2 pore size distribution data above. This suggests that in the Pt/3% Zr-ECS catalyst, relatively more Pt is deposited inside the micro- and mesopores away from contact with the sulfonic acid group in the ionomer, which can decrease ORR kinetics.[39]

CHEMICAL STATE OF ZIRCONIUM

The oxidation state and chemical structure of Zr were evaluated using ex situ XPS of the powder samples and in situ X-ray absorption near edge structure (XANES). XANES is a bulk-averaged technique, whereas XPS is a surface-sensitive measurement. Figure 4c shows the Zr 3d XPS of the 3% Zr-ECS predoped sample and the corresponding Pt/3% Zr-ECS catalyst (see also Figure S6). On the 3% Zr-ECS carbon, Zr 3d XPS shows well-resolved doublet peaks due to spin−orbit coupling at 182.9 and 185.2 eV (Δ_{Zr} = ~2.3 eV), confirming the presence of Zr in the +4 oxidation state with a possible chemical form ZrO_2.[42] On the Pt/3% Zr-ECS sample though, in addition to the doublet peak, two smaller peaks at lower binding energies of 179.9 and 182.2 eV are also observed, indicating the presence of Zr in a slightly reduced chemical form as zirconium suboxide (Zr^{n+}, $n < 4$, ZrO_{2-x}).[43] As shown in Figure S6, no shift in the 4f binding energy of Pt is observed upon ZrO_2 deposition, suggesting that ZrO_2 is physically interacting with only Pt.

Figure 4d shows the in situ Zr K-edge XANES profiles, and their derivatives, for the Pt/3% Zr-ECS sample compared to that of Zr metal and ZrO_2 standard compounds (also see Figure S7). The XANES edge profile of Zr in the catalyst is similar to monoclinic ZrO_2 (m-ZrO_2) with a characteristic broad asymmetric single-peak white line and is consistent with 7- or 8-coordinate Zr with multiple nearest neighbor bond lengths.[44,45] The XANES edge position of Zr in the catalyst is shifted negatively to 18,011 eV compared to m-ZrO_2 (18,012), indicating that Zr is in a reduced chemical state (Zr^{n+}, $n < 4$) in good agreement with XPS results. The Pt L3-edge XANES profile in Figure 4e shows a marginal decrease in the white line for Pt/3% Zr-ECS compared to Pt/ECS indicating the presence of ZrO_{2-x} on the surface of Pt nanoparticles. The extended X-ray absorption fine structure (EXAFS, see Figures S8 and S9 and Table S3) fits at 0.5 V in situ, suggesting a similar coordination number (8.8 ± 0.4 for Pt/3% Zr-ECS vs 9.4 ± 0.3 for Pt/ECS) and Pt−Pt bond length (2.747 ± 0.003 for Pt/3% Zr-ECS vs 2.745 ± 0.002 for Pt/ECS) within the error levels of the measurement.

FUEL CELL PERFORMANCE AND DURABILITY

The novel Pt/3% Zr-ECS catalyst was evaluated in a 5 cm^2 active area fuel cell MEA under differential cell conditions for its performance and durability compared to nondoped ECS at 0.2 mg$_{Pt}$/cm^2 loading (Figures 5 and S9). The catalyst-specific durability measurement was performed by subjecting the cathode to 90,000 voltage cycles from 0.60 to 0.95 V at 90 °C, 100% RH, and 104 kPa in N_2 environment. As shown in Figure 5a, Pt/3% Zr-ECS catalyst shows significantly improved cell voltage retention after 90,000 cycles both in the kinetic and mass-transport limited regions. At BOL in the kinetic region, the Pt/3% Zr-ECS catalyst exhibits 0.887 mV at 0.05 A/cm^2, which is ~15 mV higher than that of the Pt/ECS catalyst. This benefit reflects the higher mass activity of 0.49 A/mg$_{Pt}$ for Pt/3% Zr-ECS, which exceeds the DOE target of >0.44 A/mg$_{Pt}$ with a pure-Pt catalyst in an MEA,[1] compared to 0.36 A/mg$_{Pt}$ for the Pt/ECS catalyst. This is due to the presence of a larger fraction of Pt nanoparticles inside the mesopores of the Zr-doped carbon support, compared to the nondoped ECS, preventing adsorption of sulfonate anions from the ionomer that poison the ORR leading to a higher specific activity of 747 ± 7 μA/cm$^2_{Pt}$ for Pt/3% Zr-ECS compared to 559 ± 31 μA/

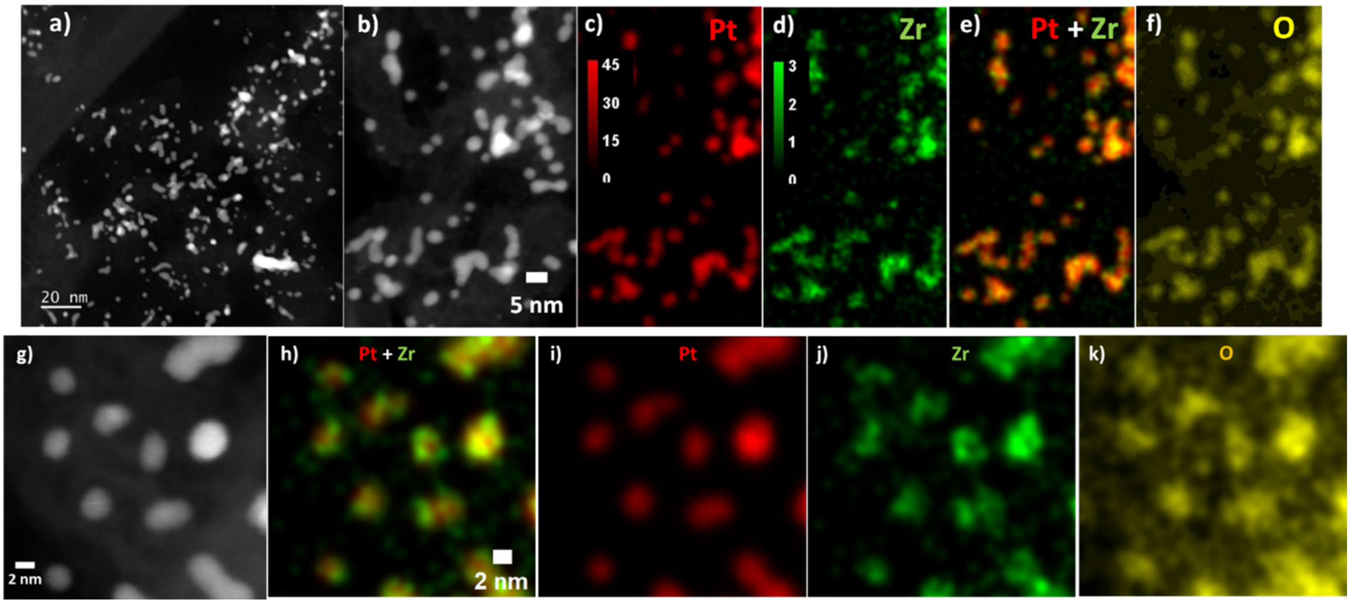

Figure 6. (a, b, g) HAADF STEM images and (c−f, h−k) EDS maps of the elements in Pt/3% Zr-ECS (predoped and heat treated) catalyst at EOT after 30,000 AST voltage cycles in an MEA.

cm^2_{Pt} for Pt/ECS (Figure S10). This kinetic benefit was maintained throughout the 90,000 AST cycles with better retention in mass activity of 61% for Pt/3% Zr-ECS vs 50% for Pt/ECS catalyst. This was also reflected in the higher cell voltage of 0.874 mV at 0.05 A/cm^2 for Pt/3% Zr-ECS at EOT. The importance of ZrO_{2-x} nanocluster surface decoration was reflected in the cell voltage durability at high-current density and the improved retention of Pt ECSA. At BOL, both the catalysts show similar cell voltages of ~0.660 V at 2.0 A/cm^2 and ECSAs of ~66 m^2/g. As the durability cycling progressed, the Pt ECSA showed improved retention on Pt/3% Zr-ECS catalyst and was better than Pt/ECS by ~26% after 90,000 AST cycles. The initial drop over the first 30,000 AST cycles still dominated both materials, although it was observed to be better on the Pt/3% Zr-ECS catalyst. ECSA was measured to be 24 m^2/g for Pt/3% Zr-ECS compared to 19 m^2/g for Pt/ECS after 90,000 AST voltage cycles. This was reflected in the remarkably higher cell voltage retention, as shown in Figure 5c. Pt/ECS catalyst loses ~55 mV at 2.0 A/cm^2 with most of the loss coming in the first 30,000 AST voltage cycles. In comparison, Pt/Zr-ECS loses only 20 mV at 2.0 A/cm^2 after 90,000 AST cycles maintaining 0.640 V at EOT with a shallower profile in voltage loss.

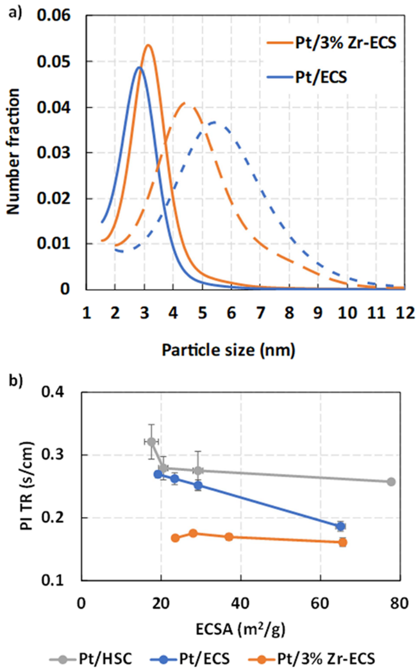

Figure 7. (a) SAXS Pt particle size distribution (solid lines − BOL, dashed lines − EOT after 30,000 AST cycles) and (b) pressure-independent O_2 transport resistance as a function of cathode ECSA up to 90,000 AST cycles; also, shown is the 30% Pt/HSC catalyst for comparison.

■ POSTCHARACTERIZATION OF THE CATALYST

Figure 6a−k shows the STEM-EDS images of the Pt/3% Zr-ECS catalyst after 30,000 AST cycles in a PEMFC MEA (see Figure S2b,c for STEM images of the Pt/ECS catalyst after AST cycles). Both Pt/ECS and Pt/3% Zr-ECS catalysts appeared to have coarsened via migration-coalescence, as seen by the formation of fused and elongated Pt nanoparticles on the carbon support. The ZrO_{2-x} nanoclusters continue to be associated with the Pt nanoparticles mostly present on and around them (Figure 6g−o). A marginal increase in the Pt/Zr atomic ratio to 9.2 ± 1.1 is observed with the atomically dispersed Zr completely lost after AST voltage cycling. Pt particle size distributions (PSD) were determined using small-angle X-ray scattering measurement (SAXS) as shown in Figure 7a and were obtained from fitting the scattering data in the q region between 0.02 and 0.4 Å^{-1} using the maximum entropy (MaxEnt) method (Figure S11). The pristine Pt/ECS and Pt/Zr-ECS catalyst layers showed similar Pt particle mean diameters of 2.5 and 2.7 nm, respectively. After 30,000 voltage cycles, the Pt mean particle diameters for both the Pt/ECS and Pt/3% Zr-ECS catalyst increased and the PSDs broadened after AST cycling with a longer tail signifying particle coarsening via migration-coalescence (Figure 6a,b).[20,21,46] The mean Pt particle size after AST cycles for the nondoped Pt/ECS catalyst is 5.5 nm, which is larger than the 4.5 nm for the doped Pt/3% Zr-ECS catalyst, indicating that ZrO_{2-x} surface nanoclusters mitigate Pt coarsening during fuel cell testing, in good agreement with the improved ECSA retention. The number fraction of particles also shows a distinctly long tail at larger particle sizes due to the presence of elongated particles. We attribute this feature to the slightly higher degree of ordering in the carbon planes for ECS supports and the larger primary particles of the support featuring a more continuous internal surface. This is also in good agreement with the electrochemical CO_{ad} stripping of Pt/ECS and Pt/3% Zr-ECS catalysts in an MEA that does not show any change in Pt utilization after 30,000 AST cycles, indicating that the Pt nanoparticles mostly remain inside the mesopores of ECS-based supports (Figure S12). Pt dispersed on graphitized support with a higher degree of order in the carbon planes has previously been shown to coarsen via migration-coalescence with the formation of elongated particles as the dominant mechanism.[20,21,46]

O_2 REACTANT TRANSPORT CHARACTERISTICS

Figure 7b shows a plot of the pressure-independent O_2 transport resistance measured from the limiting current density measurements. Pressure-independent transport resistance largely arises due to the (i) Knudsen diffusion of O_2 in the small pores (<10 nm) of the microporous layer of the cathode gas diffusion layer and the cathode catalyst layer and (ii) diffusion of O_2 in the thin ionomer layer of the cathode catalyst layer.[1] Pressure-independent transport resistance is (i) a strong function of the cathode Pt surface area and increases with decreasing ECSA as the catalyst ages[47,48] and (ii) dependent on the pore structure of the carbon support with more open, mesopores facilitating O_2 transport properties.[49,50] The pressure-independent transport resistance of Pt/3% Zr-ECS catalyst is lower (0.16 s/cm at a BOL Pt ECSA of $\sim$66 m^2/g_{Pt}) due to the open, mesoporous structure of the carbon support that enables improved accessibility of the O_2 to Pt nanoparticles and remains stable in the range of 0.16 to 0.18 s/cm as the Pt ECSA decreases to 24 m^2/g after 90,000 voltage cycles. The Pt/ECS catalyst also shows a lower pressure-independent transport resistance value of 0.19 s/cm at BOL due to the mesoporous character of the support but drastically increases to 0.27 s/cm after 90,000 AST cycles. On the contrary, the pressure-independent transport resistance of a commercially available 30% Pt/HSC catalyst begins high at 0.26 s/cm due to its dominant pore structure with smaller micropores, which remains constant but then increases drastically to 0.32 s/cm after 90,000 AST-cycles with ECSA decreasing to $\sim$18 m^2/g.

Characterization of the catalysts was performed to determine the influence of ZrO_{2-x} doping on the Pt nanoparticles stability during potential cycling of the electrode via online inductively coupled plasma mass spectrometry (Figure S13). Measurements were carried out in N_2 saturated 0.1 M $HClO_4$ electrolyte to understand the stability of the catalysts toward Pt dissolution reactions. As shown in Figure S13, no difference was observed between Pt/ECS and Pt/Zr-ECS catalysts neither in anodic oxidative nor the cathodic reductive sweeps (0.40 to 0.95 V region). This indicates that the presence of atomically dispersed Zr and/or the ZrO_{2-x} nanocluster on Pt does not inhibit the Pt dissolution reactions. Further, electrochemical CO_{ad} stripping was carried out on the catalysts in aqueous 0.1 M $HClO_4$, which suggested no influence of a-Zr and ZrO_{2-x} nanoclusters on the oxidation of CO adsorbed on the Pt nanoparticles (Figure S14). These observations suggest that a-Zr and ZrO_{2-x} nanoclusters likely do not exert any chemical or electronic influence sufficient to change Pt dissolution behavior or oxidative CO_{ad} stripping characteristics.

ZrO_{2-x} surface decorating nanoclusters appear to physically anchor Pt nanoparticles to the carbon support or stabilize the loosely coordinated edge atoms, thereby mitigating Pt surface area loss. Based on the N_2 adsorption pore size analysis, atomically dispersed Zr was largely observed to increase the micro- and mesoporosity of the ECS support, thereby enabling the Pt nanoparticle dispersion away from the ORR-inhibiting perfluorosulfonic acid ionomer and increasing mass activity. The enhanced mesoporous structure of the engineered carbon support enabled improved O_2 transport properties of the electrode even on the degraded catalyst layer with low Pt surface area. This combination of better retention of mass activity, ECSA, and pressure independent O_2 transport resistance enabled a higher cell voltage at EOT for a PEMFC MEA with a cathode catalyst of Pt surface-decorated by ZrO_{2-x} nanoclusters.

SUMMARY

A catalyst comprising Pt nanoparticles surface-decorated with ZrO_{2-x} nanoclusters and supported on porous engineered carbon featuring atomically dispersed Zr metal sites was synthesized and utilized as the cathode catalyst in a PEMFC MEA. Surface decorating ZrO_{2-x} nanoclusters were serendipitously formed on and around the Pt nanoparticles during the heat treatment step and acted as anchoring agents to reduce the coarsening of Pt and improve its surface area retention. ZrO_{2-x} nanoclusters appeared to interact with Pt physically by either anchoring it to the carbon and/or healing the loosely coordinated Pt edge atoms. The higher kinetic activity due to Pt being inside the mesopores and not poisoned by the ionomer and the better ECSA retention and lower O_2 transport resistance led to significantly improved durability in cell voltage across the entire polarization curve. We have thus delineated the structure and electrochemical properties of a novel Pt catalyst with surface-decorating ZrO_{2-x} nanoclusters that improve PEMFC durability.

METHODS

Materials and MEA Fabrication. Engineered Catalyst Support, namely ECS3701 (labeled in short form as ECS), a commercially available carbon support, is produced by Pajarito Powder using their VariPore technology.[33−35,51,52] ECS, Zr-ECS, and Pt/Zr-ECS follow a similar synthesis process as briefly described here. The general Zr-ECS production method involves a mixture of a nitrogen-rich organic precursor such as melamine, fumed silica, and zirconium nitrate salt as a zirconium precursor that is then pyrolyzed at high temperatures. The silica template is removed with hydrofluoric acid, resulting in an engineered carbon support structure. This carbon support is then washed with copious water, dried, and heat treated under a controlled atmosphere at 800 °C in a nitrogen atmosphere. Additional zirconium is deposited onto the carbon support using the Zr precursor followed by heat treatment to form Zr-ECS. Platinum is then chemically deposited onto the surface pores of the Zr-ECS at 30 or 50 wt % nominal loading. The Pt/Zr-ECS3701 is then washed, dried, and heat treated under a controlled atmosphere to ensure complete deposition. ECS carbon and Pt/ECS followed similar procedures but in the absence of a Zr precursor. Pt catalyst at 30 and 50% nominal loading was also deposited on a high surface area carbon support, namely, the KetjenBlack EC-300J as a baseline.

A catalyst-coated membrane (CCM) electrode assembly with a 5 cm^2 active area was used to test the electrode designs fabricated in this study.[47,53] A 20 wt % Pt/C electrocatalyst was used on the anode. The Pt loadings in the anode and cathode were 0.05 and 0.2 mg_{Pt}/cm^2. Cathode catalyst inks were made by dispersing the catalyst in an n-propanol to water (3:1) solvent mixture featuring a short side chain PFSA ionomer and an equivalent weight of 800 g mol^{-1}. The ionomer to carbon ratios were optimized at 0.9 for Pt/HSC and 1.0 for Pt/ECS, and Pt/Zr-ECS electrodes. An ionomer-to-carbon ratio of 0.6 was used to fabricate the anode. A roughly 230 μm thick carbon fiber paper-based gas diffusion layer containing a microporous layer was used on both the anode and cathode sides. A 12 μm thick PFSA membrane with mechanical reinforcement was used for the MEA lamination, which was carried out at 145 °C temperature, 5000 lbs. of force for a duration of 2 min.

Physical Characterization. Brunauer−Emmett−Teller (BET) and Barrett−Joyner−Halenda (BJH) analyses were used to measure the specific surface area and pore size distribution of the carbon powders. The measurements were taken using an ASAP 2020 physisorption system from Micromeritics Instrument Corporation. Additional details regarding BET and BJH measurements can be found in our previous publication.[50] Volumetric water uptake measurements were done at room temperature (25 °C) using a Micromeritics 3Flex DVS apparatus by ramping up the relative water vapor pressure in steps up to 80% while measuring the quantity of water adsorbed at each step.

XPS spectra were collected using a Thermo Scientific NEXUS G2 with a primary X-ray source of microfocused, monochromatic Al K-alpha X-rays. For all survey and high-resolution scans, a raster spot size of 400 μm × 400 μm was used. All survey spectra were analyzed with a pass energy of 200 eV and a step size of 1.0 eV while high-resolution spectra of C 1s, O 1s, N 1s, and S 2p were collected with a pass energy of 50 eV and a step size of 0.05 eV. All data analysis was performed on Thermo Avantage software. Quantification was performed using an iterative/convergence model using the Gaussian-Lorentian peak shape, Shirley background, and Wagner-Scofield relative sensitivity factors.

The diffraction data were collected using the Bruker D8-Advance X-ray Diffractometer system with the Bragg−Brentano geometry and Cu Kα radiation (40 kV and 40 mA). Samples were prepared by dusting powder onto a quartz zero-background holder coated with a thin layer of grease to promote adhesion. Phase identification was performed by comparing the observed diffraction patterns to reference data from the International Centre for Diffraction Data (ICDD).[54] Raman spectra were collected on carbon powders with a Renishaw inVia confocal microscope spectrometer. Samples were probed with a 532 nm excitation line using a 50× objective ~1 μm^2 spot size with a spectral resolution of 2 cm^{-1}. Peak parameters were attained from curve fits based on mixed Gaussian and Lorentzian curves.

Electron Microscopy. STEM experiments were performed using Thermo-Fisher Titan Themis Cryo S/TEM with a Field Emission Gun (X-FEG), monochromator, and probe corrector operated at 120 kV and room temperature. The High-Annular Angle Dark Field (HAADF) and Bright Field (BF) images were collected with 195 mm camera length and a 21.4 mrad convergence angle. The HAADF images were taken with 2048 × 2048 pixels and 2~5 μs dwell time.

Electrochemical Diagnostics. Electrochemical diagnostic measurements comprising ECSA, mass activity, specific activity, local-O_2 transport resistance ($R(O_2)$-local), Pt utilization via electrochemical CO_{ad} stripping, and polarization curves were obtained by testing the MEAs in a 5 cm^2 differential cell. Initially, MEAs were conditioned for 24 h before proceeding with the polarization curve and electrochemical diagnostic measurements. The MEA conditioning protocols were described in a previous publication.[55]

Hydrogen adsorption−desorption measurements (HAD) were done after MEA conditioning using cyclic voltammetry (CV) to calculate the ECSA. The cathode and anode were fed with pure N_2 and H_2 gases simultaneously. The CV scan was made between 0.05 and 1.0 V using a scan rate of 20 mV/s under no N_2 flow in the cathode and 0.2 slpm H_2 in the anode. A total of 4 CV scans were done and the fourth scan was used to calculate the ECSA between 0.05 and ~0.4 V. Kinetic activity measurements were done by flowing pure hydrogen and oxygen into the anode and cathode, respectively. Polarization curves ranging from current densities between 0.02 and 0.40 A/cm^2 were measured at 80 °C and 100% RH with an absolute anode−cathode outlet pressure of 150 kPa. The mass activity at 0.9 V was measured from the Tafel plot (semilog plot of voltage versus current density). The voltage measured was corrected for the ohmic resistance, while the current density was corrected for H_2 crossover and shorting resistance.

$R(O_2)$-local was measured by conducting limiting current measurements at various total pressures with different low oxygen partial pressures. The limiting current densities were measured at several potentials below 0.3 V at different oxygen mole fractions (1 to 4%). The slope from the plot between the limiting current density and oxygen mole fraction yields the total transport resistance. The total transport resistances were obtained at different cathode outlet pressures (100 to 300 kPa). Next, total transport resistances were plotted versus cathode outlet pressures from which the slope and intercept extracted represent pressure-dependent and pressure-independent transport resistance, respectively.[47,56]

Pt utilization of the electrodes was determined by conducting CO stripping measurements at 80 °C. CO stripping involves electrooxidation of adsorbed CO on the Pt surface ($Pt\text{-}CO_{ads} + H_2O \rightarrow Pt + CO_2 + 2H^+ + 2e^-$).[38,57] Initially, the cathode was purged with nitrogen (N_2) gas for 1 min, and then several CV scans between 0.05 and 1.2 V were performed to clean the electrode surface. Next, the cathode was saturated with 1% CO (balance N_2) for 15 min. The flow rate of the CO was 1 slpm. Finally, N_2 was flowed into the cathode again for 1 min and CO stripping was carried out by performing a CV scan between 0.05 and 0.95 V. Pure H_2 was flowed into the anode for the entire measurement. The CO stripping measurement for each electrode was done at RH values ranging between 10 and 100%. ECSA from the CO stripping measurement was calculated by integrating the CO electrooxidation peak, assuming a charge density of 420 $\mu C/cm^2$. The ratio of ECSA at each RH was normalized to that obtained at 100% RH to calculate the Pt utilization. The electrochemical oxidation of CO_{ad} is reliant on access to water according to the equation $Pt\text{-}CO_{ad} + H_2O \rightarrow Pt + CO_2 + 2H^+$

+ 2e$^-$ and hence is dependent on the RH of operation. Under a relatively dry condition of 20% RH, Pt nanoparticles present inside the micro/mesopores of the carbon particles are not accessed. Further, the Pt dry accessibility also depends on the continuity of the ionomer films dispersed on the carbon support with more continuous ionomer films connecting more Pt ionically. Discontinuous ionomer films will require condensed water on the carbon catalyst to connect the ionomer patches.[49,50] Hence, the dry accessibility or utilization at 20% RH represents the fraction of Pt present on the external surface of the carbon in direct contact with the continuous layer of the ionomer.

Fuel cell polarization curves were obtained by flowing H_2/air on anode/cathode channels at 94 °C and at an absolute outlet pressure of 250 kPa and an inlet RH of 100%. The catalyst-specific AST involves trapezoidal wave cycling between 0.6 and 0.95 V in H_2/N_2 anode/cathode gas flows at 90 °C, 104 kPa outlet pressure, and 100% RH. The hold times at 0.6 and 0.95 V were 1 and 2 s, respectively, and the ramp times in both anodic and cathodic directions were 0.5 s each. The total time for each cycle is 4 s. A total of up to 90,000 cycles was run as a part of the AST. The polarization curves along with kinetic activities and ECSA were measured before and after the AST to monitor the performance degradation of the electrodes.

X-ray Scattering and Absorption Studies. The structure of Pt/ECS and Pt/Zr-ECS electrodes before and after durability testing was characterized using X-ray scattering at beamline 9ID-C at the Advanced Photon Source (APS) at Argonne National Laboratory. The samples were exposed to a 16.8−21 keV monochromatic X-ray beam and the scattered X-ray intensities were measured using a Bonse−Hart camera for the USAXS region and a Pilatus 100 K detector for pinhole SAXS and WAXS. The scattering vector, q, of the measurement ranges between 10^{-4} and 2×10^{-2} Å^{-1} for USAXS and 2×10^{-2} and 4×10^{-2} Å^{-1} for pinhole SAXS. The scattering vector is the inverse of the object size, given as $q = 4\pi \sin(\theta/2)/\lambda$, where λ is the wavelength of the X-ray beam. Based on the q range, the measurement length scale spans between 1 nm and approximately 1 μm. The WAXS data covered a d-spacing range from approximately 6.0 to 0.8 Å. The background scattering data of the substrates used to support the samples were also collected and subtracted from the subsequent scattering data for each sample. The data were reduced with the NIKA software package,[58] and data analysis was conducted using the IRENA software package.[59] Both packages were run on an IGOR Pro 8.0 instrument (Wavemetrics). Particle size distribution was obtained from the measured scattering data using the maximum entropy (MaxEnt) method,[60] which involves a constrained optimization of parameters to solve the scattering equation

$$I(q) = |\Delta\rho|^2 \int |F(q, r)|^2 (V(r))^2 N_p(r) dr$$

where $I(q)$ is the scattered intensity, ρ is the scattering length density of the particle, $F(q, r)$ is the scattering function at scattering vector q of a particle of characteristic dimension r, V is the volume of the particle, and N_p is the number density of particles in the scattering volume.

XAS measurements were made at the APS at Materials Research Collaborative Access Team (MRCAT) beamline 10-ID. The energy was selected with a liquid nitrogen-cooled Si(111) crystal pair, while harmonic rejection was accomplished with a rhodium-coated mirror. Zr K edge spectra were collected in fluorescence mode using a Sr filter (EXAFS Materials) and Soller slits (The EXAFS Company) to filter the elastic scatter and background Pt fluorescence, while the Pt L_3 edge spectra were measured in fluorescence using a Zn filter and Soller slits. Zr foil reference spectra were measured simultaneously during the in situ experiment and the energy was calibrated to the zero-crossing of the second derivative at 17,995.88 eV, while Pt L_3 spectra were calibrated assigning the zero-crossing of the second derivative to 11,562.76 eV. The Zr K edge transmission edge step ($\Delta\mu x$) of the electrode was about 0.006. Data were processed and fit using the Demeter/Athena/Artemis software suite.[61]

Online inductively coupled plasma mass spectrometry (ICP-MS) dissolution experiments were performed using a custom-made electrochemical flow cell (glassy carbon working electrode, high surface area carbon paper counter electrode, and a flexible Dri-ref Ag/AgCl reference electrode) with a 0.381 mm thick PTFE gasket (three layers of 127 μm thick PTFE sheet). The flow cell coupled with an Agilent 7500ce ICP-MS instrument (Agilent Technologies, Palo Alto, California, USA) equipped with an inert perfluoroalkyl (PFA) sample introduction system that includes a PFA microflow nebulizer, Peltier-cooled PFA double pass Scott-type spray chamber, connecting tube, and an inert sapphire injector fitted to a semidemountable quartz torch. A forward radio frequency power of 1500 W was used with the following Ar gas flows: carrier 0.9 L min^{-1}, makeup 0.15 L min^{-1}, and plasma gas 15 L min^{-1}. The Pt and Zr ICP-MS signals were measured at a mass/charge (m/z) of 195 and 90 amu, respectively, using 0.5 s integration time per point. Electrochemical experiments were performed using air-equilibrated 0.1 M perchloric acid ($HClO_4$) (GFS Chemicals, Inc.; 18 MΩ Millipore water) electrolyte which was pumped into the flow cell at a rate of 0.183 mL min^{-1}, using the ICP-MS peristaltic pump, and directly into the nebulizer of the ICP-MS. The ICP-MS was tuned for high sensitivity to obtain the best possible signal-to-noise ratio for the measurements. To perform quantitative analysis, a blank of 0.1 M HClO4 and standard solutions of Pt−Zr (0, 0.5, 1, and 2 ppb) in 0.1 M $HClO_4$ were analyzed before the electrochemical dissolution experiments. Calibration curves were created from the ICP-MS signals for these standards to convert the ICP-MS count rate to absolute concentrations in the electrolyte. Potential-dependent dissolution experiments using the custom electrochemical flow cell were performed using a Solartron single-channel potentiostat (SI 1287, Solartron Instruments) and a silver/silver chloride reference electrode (Dri-ref, FLEXREF 1.5 mm) with a flexible wire connector. The counter electrode was carbon paper, and the working electrode was the dried Pt/ECS and Pt/Zr-ECS thin film ink deposited on a 0.196 cm^2 geometric area custom-made glassy carbon (GC) disk embedded in a PTFE sleeve. Electrode loading was 4 μg_{Pt}/cm^2 loading, and the ink on the GC was dried while rotating the electrode at 500 rpm. The reference electrode was calibrated against a reversible hydrogen electrode (RHE) and all potentials reported here are with respect to RHE.

The catalyst-ionomer ink composition and preparation procedure for the XAS measurements were the same as those used for the online ICP-MS experiments. The ink was deposited on a rectangular graphene sheet entirely encased in Kapton tape, except for three 5 mm × 3 mm rectangles in the middle of the graphene sheet and a strip at the end of the sheet. The catalyst-ionomer ink was deposited in these three rectangles to achieve Pt loadings of 0.5 mg_{Pt}/cm^2 for Pt/ECS and 3 mg_{Pt}/cm^2 for Pt/Zr-ECS. The graphene sheet and catalyst layers were sealed against a 10 mL cavity in a PEEK cell containing a carbon paper counter electrode and Ag/AgCl reference electrode. (BASi MW-2030, 3 M NaCl). Argon-purged 0.1 M $HClO_4$ was circulated through the cell at ∼50 mL min^{-1} by using a peristaltic pump during the acquisition of the XAS spectra. The Ag/AgCl reference electrode was calibrated against a reversible hydrogen electrode (RHE) in hydrogen-saturated 0.1 M $HClO_4$. All potentials in the remainder of the article have been converted to the RHE scale. A CH Instruments potentiostat was used to control the potential of the electrodes, and *iR* compensation was used during the measurements. XAFS spectra were acquired in the sequence: open circuit potential (0.993 V), 0.1 0.3, 0.5, 0.7, and 0.9 V.

■ ASSOCIATED CONTENT

Supporting Information

The Supporting Information is available free of charge at https://pubs.acs.org/doi/10.1021/acscatal.3c05297.

> Physicochemical characterization of the catalysts, pore size distribution, HAADF-STEM images, EDS mapping, water uptake, XPS characterization, details on XAS experiments, and fitting results, electrochemical CO stripping, and ICP-MS results (PDF)

■ AUTHOR INFORMATION

Corresponding Author

Nagappan Ramaswamy − *Global Fuel Cell Business, General Motors LLC, Pontiac, Michigan 48340, United States;* orcid.org/0000-0002-3430-2758; Email: Nagappan.Ramaswamy@gm.com

Authors

Zixiao Shi − *Department of Chemistry and Chemical Biology, Cornell University, Ithaca, New York 14853, United States*

Barr Zulevi − *Pajarito Powder, Albuquerque, New Mexico 87109, United States;* Present Address: Electric Hydrogen, 3 Strathmore Rd, Natick, Massachusetts 01760, United States (B.Z.)

Geoff McCool − *Pajarito Powder, Albuquerque, New Mexico 87109, United States*

Nathan P. Mellott − *Global Fuel Cell Business, General Motors LLC, Pontiac, Michigan 48340, United States*

Anusorn Kongkanand − *Global Fuel Cell Business, General Motors LLC, Pontiac, Michigan 48340, United States*

Swami Kumaraguru − *Global Fuel Cell Business, General Motors LLC, Pontiac, Michigan 48340, United States*

Michele L. Ostraat − *Pajarito Powder, Albuquerque, New Mexico 87109, United States*

David A. Muller − *School of Applied and Engineering Physics, Cornell University, Ithaca, New York 14853, United States; Kavli Institute at Cornell for Nanoscale Science, Ithaca, New York 14853, United States;* orcid.org/0000-0003-4129-0473

Nancy N. Kariuki − *Chemical Sciences and Engineering Division, Argonne National Laboratory, Lemont, Illinois 60439, United States*

Deborah J. Myers − *Chemical Sciences and Engineering Division, Argonne National Laboratory, Lemont, Illinois 60439, United States;* orcid.org/0000-0001-9299-3916

A. Jeremy Kropf − *Chemical Sciences and Engineering Division, Argonne National Laboratory, Lemont, Illinois 60439, United States;* orcid.org/0000-0002-3329-4493

Complete contact information is available at: https://pubs.acs.org/10.1021/acscatal.3c05297

Author Contributions

N.R. led the project, provided guidelines for synthesis and characterization, performed fuel cell experiments, analyzed data, and wrote the manuscript. N.P.M. performed XPS measurements and analyzed data. A.K. and S.K. supervised the project and assisted in writing the manuscript. B.Z. supervised the project at Pajarito Powder LLC providing synthesis guidelines and GM synthesized the catalyst materials. M.L.O. supervised the project at Pajarito Powder LLC and revised the manuscript. D.A.M. supervised the project at Cornell University and Z.S. performed the electron microscopy measurements and analyzed the results. D.J.M. supervised the project at Argonne, N.N.K. performed and analyzed SAXS, and ICP experiments, and A.J.K. performed and analyzed XAS measurements.

Funding

This work was partially supported by the U.S. Department of Energy (DOE), Hydrogen and Fuel Cell Technologies Office (HFTO) under grant DE-EE0008821. Cornell work was supported by the electron microscopy facility from the Cornell Center for Materials Research under NSF Grant DMR-1719875. The Argonne work was supported by the U.S. DOE HFTO through the Million Mile Fuel Cell Truck Consortium (M2FCT). SAXS and XAFS measurements used the resources of the Advanced Photon Source (APS), a U.S. DOE Office of Science User Facility operated for the DOE Office of Science by Argonne National Laboratory under Contract No. DE-AC02−06CH11357. XAFS data were acquired at the MRCAT of the APS; MRCAT operations are supported by the Department of Energy and the MRCAT member institutions.

Notes

The authors declare no competing financial interest.

■ ACKNOWLEDGMENTS

N.P.M. would like to acknowledge Nicholas Pieczonka and Francesca Stephenson at GM Warren Technical Center for providing Raman and XRD characterization of supports. N.R. would like to acknowledge Kenneth Holt, Mackenzie Benning, Melanie Molotky, Kathryn Stevick, and April Vaughter at GM Pontiac Engineering Center for fabrication, analytical and engineering support at GM. SAXS data were acquired at beamline 9-ID at the APS. The authors thank Jan Ilavsky and Ivan Kuzmenko of APS 9-ID for assistance with the SAXS measurements.

■ REFERENCES

(1) Kongkanand, A.; Mathias, M. F. The Priority and Challenge of High-Power Performance of Low-Platinum Proton-Exchange Membrane Fuel Cells. *J. Phys. Chem. Lett.* **2016**, *7* (7), 1127−1137.

(2) Gröger, O.; Gasteiger, H. A.; Suchsland, J.-P. Review—Electromobility: Batteries or Fuel Cells? *J. Electrochem. Soc.* **2015**, *162* (14), A2605.

(3) Sun, Y.; Polani, S.; Luo, F.; Ott, S.; Strasser, P.; Dionigi, F. Advancements in cathode catalyst and cathode layer design for proton exchange membrane fuel cells. *Nat. Commun.* **2021**, *12* (1), 5984.

(4) Shao, Y.; Dodelet, J.-P.; Wu, G.; Zelenay, P. PGM-Free Cathode Catalysts for PEM Fuel Cells: A Mini-Review on Stability Challenges. *Adv. Mater.* **2019**, *31* (31), 1807615.

(5) Kodama, K.; Nagai, T.; Kuwaki, A.; Jinnouchi, R.; Morimoto, Y. Challenges in applying highly active Pt-based nanostructured catalysts for oxygen reduction reactions to fuel cell vehicles. *Nat. Nanotechnol.* **2021**, *16* (2), 140−147.

(6) Cullen, D. A.; Neyerlin, K. C.; Ahluwalia, R. K.; Mukundan, R.; More, K. L.; Borup, R. L.; Weber, A. Z.; Myers, D. J.; Kusoglu, A. New roads and challenges for fuel cells in heavy-duty transportation. *Nature Energy* **2021**, *6* (5), 462−474.

(7) Gittleman, C. S.; Jia, H.; De Castro, E. S.; Chisholm, C. R. I.; Kim, Y. S. Proton conductors for heavy-duty vehicle fuel cells. *Joule* **2021**, *5* (7), 1660−1677.

(8) Miller, E. L.; Thompson, S. T.; Randolph, K.; Hulvey, Z.; Rustagi, N.; Satyapal, S. US Department of Energy hydrogen and fuel cell technologies perspectives. *MRS Bull.* **2020**, *45* (1), 57−64.

(9) Dubau, L.; Castanheira, L.; Maillard, F.; Chatenet, M.; Lottin, O.; Maranzana, G.; Dillet, J.; Lamibrac, A.; Perrin, J.-C.; Moukheiber, E.; ElKaddouri, A.; De Moor, G.; Bas, C.; Flandin, L.; Caqué, N. A review of PEM fuel cell durability: materials degradation, local heterogeneities of aging and possible mitigation strategies. *WIREs Energy and Environment* **2014**, *3* (6), 540−560.

(10) Kocha, S. S., Electrochemical Degradation: Electrocatalyst and Support Durability, in *Polymer Electrolyte Fuel Cell Degradation*, Mench, M.M.; Kumbur, E.C.; Veziroglu, T.N., Eds.; Academic Press: Boston, 2012, 89−214.

(11) Shao-Horn, Y.; Sheng, W. C.; Chen, S.; Ferreira, P. J.; Holby, E. F.; Morgan, D. Instability of Supported Platinum Nanoparticles in Low-Temperature Fuel Cells. *Top. Catal.* **2007**, *46* (3), 285−305.

(12) Cherevko, S.; Kulyk, N.; Mayrhofer, K. J. J. Durability of platinum-based fuel cell electrocatalysts: Dissolution of bulk and nanoscale platinum. *Nano Energy* **2016**, *29*, 275−298.

(13) Chen, S.; Gasteiger, H. A.; Hayakawa, K.; Tada, T.; Shao-Horn, Y. Platinum-Alloy Cathode Catalyst Degradation in Proton Exchange Membrane Fuel Cells: Nanometer-Scale Compositional and Morphological Changes. *J. Electrochem. Soc.* **2010**, *157* (1), A82.

(14) Watanabe, M.; Yano, H.; Uchida, H.; Tryk, D. A. Achievement of distinctively high durability at nanosized Pt catalysts supported on carbon black for fuel cell cathodes. *J. Electroanal. Chem.* **2018**, *819*, 359−364.

(15) Ahluwalia, R. K.; Papadias, D. D.; Kariuki, N. N.; Peng, J.-K.; Wang, X.; Tsai, Y.; Graczyk, D. G.; Myers, D. J. Potential Dependence of Pt and Co Dissolution from Platinum-Cobalt Alloy PEFC Catalysts Using Time-Resolved Measurements. *J. Electrochem. Soc.* **2018**, *165* (6), F3024.

(16) Yang, Z.; Ball, S.; Condit, D.; Gummalla, M. Systematic Study on the Impact of Pt Particle Size and Operating Conditions on PEMFC Cathode Catalyst Durability. *J. Electrochem. Soc.* **2011**, *158* (11), B1439.

(17) Papadias, D. D.; Ahluwalia, R. K.; Kariuki, N.; Myers, D.; More, K. L.; Cullen, D. A.; Sneed, B. T.; Neyerlin, K. C.; Mukundan, R.; Borup, R. L. Durability of Pt-Co Alloy Polymer Electrolyte Fuel Cell Cathode Catalysts under Accelerated Stress Tests. *J. Electrochem. Soc.* **2018**, *165* (6), F3166.

(18) Rasouli, S.; Ferreira, P.J., Understanding the Stability of Nanoscale Catalysts in PEM Fuel Cells by Identical Location TEM, in *Nanocarbons for Energy Conversion: Supramolecular Approaches*, Nakashima, N., Ed.; Springer International Publishing: Cham, 2019, 119−134.

(19) Yu, K.; Groom, D. J.; Wang, X.; Yang, Z.; Gummalla, M.; Ball, S. C.; Myers, D. J.; Ferreira, P. J. Degradation Mechanisms of Platinum Nanoparticle Catalysts in Proton Exchange Membrane Fuel Cells: The Role of Particle Size. *Chem. Mater.* **2014**, *26* (19), 5540−5548.

(20) Padgett, E.; Yarlagadda, V.; Holtz, M. E.; Ko, M.; Levin, B. D. A.; Kukreja, R. S.; Ziegelbauer, J. M.; Andrews, R. N.; Ilavsky, J.; Kongkanand, A.; Muller, D. A. Mitigation of PEM Fuel Cell Catalyst Degradation with Porous Carbon Supports. *J. Electrochem. Soc.* **2019**, *166* (4), F198.

(21) Tuaev, X.; Rudi, S.; Strasser, P. The impact of the morphology of the carbon support on the activity and stability of nanoparticle fuel cell catalysts. *Catalysis Science & Technology* **2016**, *6* (23), 8276−8288.

(22) Hansen, T. W.; DeLaRiva, A. T.; Challa, S. R.; Datye, A. K. Sintering of Catalytic Nanoparticles: Particle Migration or Ostwald Ripening? *Acc. Chem. Res.* **2013**, *46* (8), 1720−1730.

(23) Cheng, H.; Cao, Z.; Chen, Z.; Zhao, M.; Xie, M.; Lyu, Z.; Zhu, Z.; Chi, M.; Xia, Y. Catalytic System Based on Sub-2 nm Pt Particles and Its Extraordinary Activity and Durability for Oxygen Reduction. *Nano Lett.* **2019**, *19* (8), 4997−5002.

(24) Beermann, V.; Holtz, M. E.; Padgett, E.; de Araujo, J. F.; Muller, D. A.; Strasser, P. Real-time imaging of activation and degradation of carbon supported octahedral Pt−Ni alloy fuel cell catalysts at the nanoscale using in situ electrochemical liquid cell STEM. *Energy Environ. Sci.* **2019**, *12* (8), 2476−2485.

(25) Cheng, N.; Norouzi Banis, M.; Liu, J.; Riese, A.; Mu, S.; Li, R.; Sham, T.-K.; Sun, X. Atomic scale enhancement of metal−support interactions between Pt and ZrC for highly stable electrocatalysts. *Energy Environ. Sci.* **2015**, *8* (5), 1450−1455.

(26) Kumar, A.; Ramani, V. Strong Metal−Support Interactions Enhance the Activity and Durability of Platinum Supported on Tantalum-Modified Titanium Dioxide Electrocatalysts. *ACS Catal.* **2014**, *4* (5), 1516−1525.

(27) Lu, J.; Fu, B.; Kung, M. C.; Xiao, G.; Elam, J. W.; Kung, H. H.; Stair, P. C. Coking- and Sintering-Resistant Palladium Catalysts Achieved Through Atomic Layer Deposition. *Science* **2012**, *335* (6073), 1205−1208.

(28) Takenaka, S.; Miyamoto, H.; Utsunomiya, Y.; Matsune, H.; Kishida, M. Catalytic Activity of Highly Durable Pt/CNT Catalysts Covered with Hydrophobic Silica Layers for the Oxygen Reduction Reaction in PEFCs. *J. Phys. Chem. C* **2014**, *118* (2), 774−783.

(29) Cheng, N.; Banis, M. N.; Liu, J.; Riese, A.; Li, X.; Li, R.; Ye, S.; Knights, S.; Sun, X. Extremely Stable Platinum Nanoparticles Encapsulated in a Zirconia Nanocage by Area-Selective Atomic Layer Deposition for the Oxygen Reduction Reaction. *Adv. Mater.* **2015**, *27* (2), 277−281.

(30) Yamada, H.; Kato, H.; Kodama, K. Cell Performance and Durability of Pt/C Cathode Catalyst Covered by Dopamine Derived Carbon Thin Layer for Polymer Electrolyte Fuel Cells. *J. Electrochem. Soc.* **2020**, *167* (8), No. 084508.

(31) Bardi, U.; Ross, P. N. Site blocking effect of zirconium oxide deposited on the platinum(001) single crystal surface. A study by low-energy electron diffraction, Auger electron spectroscopy, and carbon monoxide thermal desorption. *Langmuir* **1993**, *9* (1), 132−135.

(32) Ramaswamy, N.; Zulevi, B.; McCool, G.; Patton, N.; Shi, Z.; Chavez, A.; Muller, D. A.; Kongkanand, A.; Kumaraguru, S. Engineered Catalyst Support with Improved Durability at Higher Weight Percentage of Platinum. *J. Electrochem. Soc.* **2023**, *170* (11), No. 114503.

(33) Serov, A.; Atanassov, P. Carbendazim-based catalytic materials, 9,425,464 US Patent. 2016.

(34) Serov, A.; Atanassov, P. Materials with atomically dispersed chemical moieties, 10,619,256 US Patent. 2020.

(35) Serov, A.; Halevi, B.; Robson, M.; Patterson, W.; Artyushkova, K.; Atanassov, P.B. Cathode catalysts for fuel cell application derived from polymer precursors, 9,502,719 US Patent. 2016.

(36) Dzara, M. J.; Godoy, A. O.; Odgaard, M.; Zulevi, B.; Serov, A.; Jankovic, J.; Pylypenko, S. Physicochemical Properties of ECS Supports and Pt/ECS Catalysts. *ACS Applied Energy Materials* **2021**, *4* (9), 9111−9123.

(37) Joo, S. H.; Choi, S. J.; Oh, I.; Kwak, J.; Liu, Z.; Terasaki, O.; Ryoo, R. Ordered nanoporous arrays of carbon supporting high dispersions of platinum nanoparticles. *Nature* **2001**, *412* (6843), 169−172.

(38) Shinozaki, K.; Yamada, H.; Morimoto, Y. Relative Humidity Dependence of Pt Utilization in Polymer Electrolyte Fuel Cell

Electrodes: Effects of Electrode Thickness, Ionomer-to-Carbon Ratio, Ionomer Equivalent Weight, and Carbon Support. *J. Electrochem. Soc.* **2011**, *158* (5), B467.

(39) Padgett, E.; Andrejevic, N.; Liu, Z.; Kongkanand, A.; Gu, W.; Moriyama, K.; Jiang, Y.; Kumaraguru, S.; Moylan, T. E.; Kukreja, R.; Muller, D. A. Editors' Choice—Connecting Fuel Cell Catalyst Nanostructure and Accessibility Using Quantitative Cryo-STEM Tomography. *J. Electrochem. Soc.* **2018**, *165* (3), F173.

(40) Kaneko, T.; Ooyama, J.; Ohki, M.; Kanesaka, H.; Yoshimoto, Y.; Kinefuchi, I. Effect of ionomer swelling and capillary condensation of water on porous characteristics in cathode catalyst layers of polymer electrolyte membrane fuel cells under humidified conditions. *Int. J. Heat Mass Transfer* **2023**, *200*, No. 123491.

(41) Karan, K. PEFC catalyst layer: Recent advances in materials, microstructural characterization, and modeling. *Current Opinion in Electrochemistry* **2017**, *5* (1), 27−35.

(42) Barreca, D.; Battiston, G. A.; Gerbasi, R.; Tondello, E.; Zanella, P. Zirconium Dioxide Thin Films Characterized by XPS. *Surface Science Spectra* **2000**, *7* (4), 303−309.

(43) Azdad, Z.; Marot, L.; Moser, L.; Steiner, R.; Meyer, E. Valence band behaviour of zirconium oxide, Photoelectron and Auger spectroscopy study. *Sci. Rep.* **2018**, *8* (1), 16251.

(44) Greegor, R. B.; Blohowiak, K. Y.; Osborne, J. H.; Krienke, K. A.; Cherian, J. T.; Lytle, F. W. X-Ray Spectroscopic Investigation of the Zr-Site in Thin Film Sol-Gel Surface Preparations. *J. Sol-Gel Sci. Technol.* **2001**, *20* (1), 35−50.

(45) Finkeldei, S.; Stennett, M. C.; Kowalski, P. M.; Ji, Y.; de Visser-Týnová, E.; Hyatt, N. C.; Bosbach, D.; Brandt, F. Insights into the fabrication and structure of plutonium pyrochlores. *Journal of Materials Chemistry A* **2020**, *8* (5), 2387−2403.

(46) Park, Y.-C.; Tokiwa, H.; Kakinuma, K.; Watanabe, M.; Uchida, M. Effects of carbon supports on Pt distribution, ionomer coverage and cathode performance for polymer electrolyte fuel cells. *J. Power Sources* **2016**, *315*, 179−191.

(47) Greszler, T. A.; Caulk, D.; Sinha, P. The Impact of Platinum Loading on Oxygen Transport Resistance. *J. Electrochem. Soc.* **2012**, *159* (12), F831.

(48) Della Bella, R. K. F.; Stühmeier, B. M.; Gasteiger, H. A. Universal Correlation between Cathode Roughness Factor and H2/Air Performance Losses in Voltage Cycling-Based Accelerated Stress Tests. *J. Electrochem. Soc.* **2022**, *169* (4), No. 044528.

(49) Yarlagadda, V.; Carpenter, M. K.; Moylan, T. E.; Kukreja, R. S.; Koestner, R.; Gu, W.; Thompson, L.; Kongkanand, A. Boosting Fuel Cell Performance with Accessible Carbon Mesopores. *ACS Energy Letters* **2018**, *3* (3), 618−621.

(50) Ramaswamy, N.; Gu, W.; Ziegelbauer, J. M.; Kumaraguru, S. Carbon Support Microstructure Impact on High Current Density Transport Resistances in PEMFC Cathode. *J. Electrochem. Soc.* **2020**, *167* (6), No. 064515.

(51) Serov, A.; Atanassov, P.B. Non-PGM catalysts for ORR based on charge transfer organic complexes, 9,722,256 US Patent. 2017.

(52) Serov, A.; Atanassov, P.B.; Halevi, B.; Short, P. Non-PGM catalyst for ORR based on pyrolysed poly-complexes, 9,570,761 US Patent. 2017.

(53) Ramaswamy, N.; Kumaraguru, S.; Gu, W.; Kukreja, R. S.; Yu, K.; Groom, D.; Ferreira, P. High-Current Density Durability of Pt/C and PtCo/C Catalysts at Similar Particle Sizes in PEMFCs. *J. Electrochem. Soc.* **2021**, *168* (2), No. 024519.

(54) Gates-Rector, S.; Blanton, T. The Powder Diffraction File: a quality materials characterization database. *Powder Diffraction* **2019**, *34* (4), 352−360.

(55) Kabir, S.; Myers, D. J.; Kariuki, N.; Park, J.; Wang, G.; Baker, A.; Macauley, N.; Mukundan, R.; More, K. L.; Neyerlin, K. C. Elucidating the Dynamic Nature of Fuel Cell Electrodes as a Function of Conditioning: An ex Situ Material Characterization and in Situ Electrochemical Diagnostic Study. *ACS Appl. Mater. Interfaces* **2019**, *11* (48), 45016−45030.

(56) Baker, D. R.; Caulk, D. A.; Neyerlin, K. C.; Murphy, M. W. Measurement of Oxygen Transport Resistance in PEM Fuel Cells by Limiting Current Methods. *J. Electrochem. Soc.* **2009**, *156* (9), B991.

(57) Garrick, T. R.; Moylan, T. E.; Carpenter, M. K.; Kongkanand, A. Editors' Choice—Electrochemically Active Surface Area Measurement of Aged Pt Alloy Catalysts in PEM Fuel Cells by CO Stripping. *J. Electrochem. Soc.* **2017**, *164* (2), F55.

(58) Ilavsky, J. Nika: software for two-dimensional data reduction. *J. Appl. Crystallogr.* **2012**, *45* (2), 324−328.

(59) Ilavsky, J.; Jemian, P. Irena: Tool Suite for Modeling and Analysis of Small Angle Scattering. *Journal of Applied Crystallography - J. APPL CRYST* **2009**, *42*, 347−353.

(60) Jemian, P. R.; Weertman, J. R.; Long, G. G.; Spal, R. D. Characterization of 9Cr-1MoVNb steel by anomalous small-angle X-ray scattering. *Acta Metallurgica et Materialia* **1991**, *39* (11), 2477−2487.

(61) Ravel, B.; Newville, M. Data analysis for X-ray absorption spectroscopy using IFEFFIT. *Journal of synchrotron radiation* **2005**, *12*, 537−41.